AVHRR-derived cloudiness and surface temperature patterns over the Los Angeles area and their relationships to land use

Bénédicte DOUSSET

Graduate School of Architecture and Urban Planning
University of California Los Angeles[1]

Abstract. Eighty-four co-registered NOAA AVHRR satellite images of the Los Angeles basin were analyzed for the months of August 1984 and 1985, with the objectives of quantifying the differences between surface temperatures and co-located air temperatures, and of studying micro-climates using surface temperature and cloudiness statistics. Assuming a surface emissivity of 0.97 and ignoring atmospheric absorption, satellite temperatures were in good agreement with air temperatures at night, with a standard deviation of 1.6°C. During the day, they were biased 1.1°C warm in the morning and the late afternoon, and 5.4°C warm at 15:30 local time, in qualitative agreement with models of the planetary boundary layer. Pixels were classified as cloudless, covered with low (warm) or high (cold) clouds. At 03:40, low clouds occur over the ocean and cover the basin up to the edge of the San Gabriel mountains. They have dissipated by 14:40. Around 14:40, high clouds are found over the mountains and the desert, but not over the basin. Surface temperature is correlated with altitude. At 15:10, the 1800-m high San Gabriel mountains are ~17°C colder than the basin. Valleys are seen as warmer features crossing the mountain range. At 03:40, the south flanks of the mountains are ~3°C warmer than the basin. Downtown Los Angeles corresponds to a heat-island which follows contours of building density. Despite the 1-km resolution of the AVHRR, narrow features such as low thermal inertia freeways or high thermal inertia irrigated fields in the desert are detected (satellite infrared images, micro-climates).

1. Introduction

Existing meteorological observations, recorded over a sparse network of stations (often at suburban airports), do not have details at micro-climatic scales. Surface temperature and cloudiness data are most efficiently collected today by infrared scanners on board polar meteorological satellites, which provide surface temperature over the entire earth twice daily at a resolution of 1 km. The frequency and global extent of their coverage create new capabilities and provide accurate data directly applicable to the analysis of micro-climates.

In this paper, we analyze a series of co-registered satellite images of the Los Angeles basin for the months of August 1984 and 1985, with the following objectives: (1) understand and quantify the differences between satellite-derived surface temperatures and co-located air temperatures; 2) demonstrate that satellite-derived temperature and cloudiness statistics can yield useful informations on urban micro-climates.

The data and the processing steps are described in section 2. Air and satellite-derived temperatures are compared in section 3 (some results of this section have previously been discussed by Dousset, 1986). Statistics of cloudiness and surface temperature are presented in sections 4 and 5. Applications and future improvements of the method are discussed in the conclusion.

2. Data, processing and corrections

The images are from the Advanced Very High Resolution Radiometer (AVHRR) on board the NOAA-6, -7, -9 and -10 satellites. The AVHRR is a scanning radiometer with five spectral bands, centered at 0.62 μm (band 1), 0.91 μm (band 2), 3.74 μm (band 3), 10.8 μm (band 4) and 12.0 μm (band 5, NOAA-7 and -9 only). The measurement noise is ~0.1°C in bands 4 and 5, but can reach 1°C in band 3. The swath width on the earth is 3000 km and the ground resolution (pixel size) varies from 1.1×1.1 km^2 below the satellite to 1.5×4.0 km^2 at the swath edges. The satellites are launched at an altitude of about 800 km into near-polar sun-synchronous orbits and pass in view of any point on the earth twice daily, around 07:00 and 19:00 local time for NOAA-6 and 8, and 03:00 and 15:00 for NOAA-7 and 9.

Eighty-four images were processed at the Scripps Satellite Oceanography Facility. Their time distribution is shown in Fig. 1. They were geometrically corrected for the earth rotation and curvature and interactively registered to a common Mercator grid, the coverage of which is shown in Fig. 2. Small lakes such as Lake Perris (at [114,86] km on Fig. 7, 8 and 9) were used as reference points to obtain absolute positions accurate to ~2 pixels rms.

[1]corresponding address: Department of Meteorology, University of Hawaii at Manoa, Honolulu HI 96822.

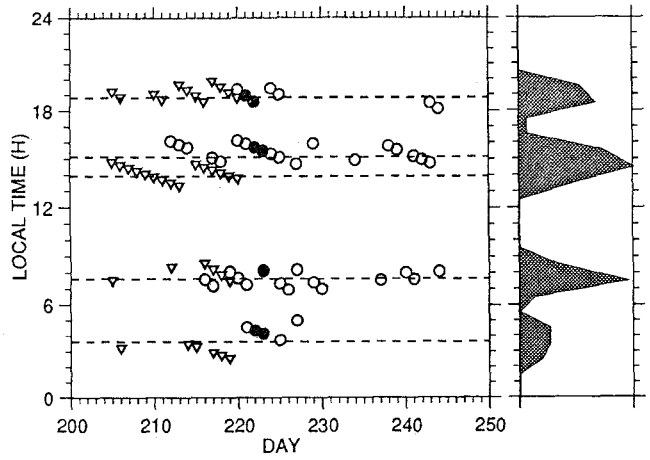

Fig. 1. Time distribution of the images. X-axis: day of the year, Y-axis: local solar time. The 1984 images are shown by circles ○ and the 1985 images by triangles ▽. The 1984 images for which in situ data are available are shown by filled circles ●. The histogram of the distribution is shown in the right panel.

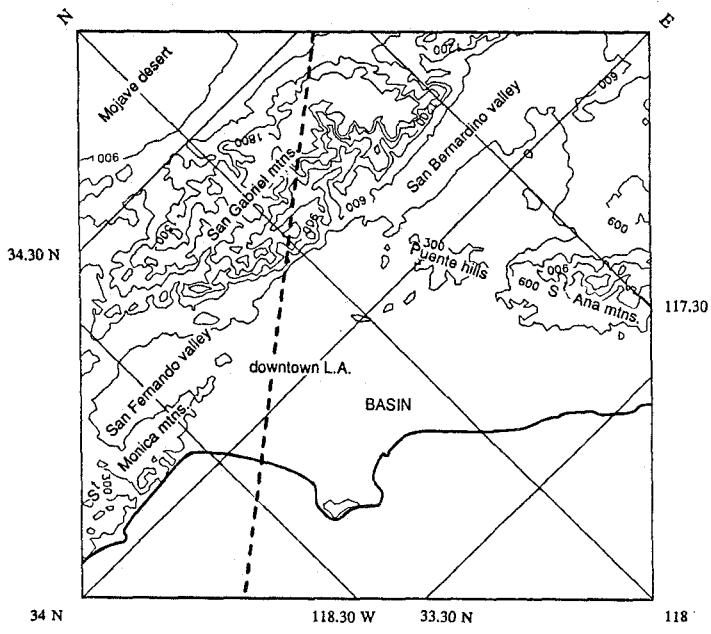

Fig. 2. Topography over the area of the images (128 km on a side). The contour lines are labeled in m above sea level. North is at the upper left of the frame. The section shown in Fig. 10 is indicated by a dashed line. Copying this figure on a transparent overlay now will facilitate the interpretation of Fig. 5 to 9.

The radiant energy in each thermal infrared band was then converted to brightness temperatures using Planck's law. In the 8 μm to 14 μm band, most natural and man-made materials found in urban areas have an emissivity smaller than the ocean (0.99) (Buetner and Kern, 1965): dry sand (0.914), wet sand (0.938), vegetation (0.975), glass (0.865), asphalt (0.958), plywood (0.962), concrete (0.966). A residential block in Los Angeles, consisting mainly of wood shingle roofs, asphalt, concrete, vegetation and pools, has an average emissivity of 0.965 to 0.97. The brightness temperature T_B is thus lower than the true surface temperature T, and, in bands 4 and 5, can be approximated by a formula derived from Planck's law:

$$T_B = T - (1-\varepsilon)\lambda T^2/C$$

where ε is the emissivity, λ is the wavelength band in m, C = $1.44 \cdot 10^{-2}$ m°K, and T and T_B are in °K. For T = 20°C, the correction is 0.6°C for each % of emissivity below 100%. Lacking detailed information on surface emissivities, we applied this correction to all the images, assuming ε = 0.97.

A surface that is not a perfect black body also reflects solar radiation (Kirchoff's law), resulting in a brightness temperature error. For a reflectance $\alpha = 1-\varepsilon = 0.03$ in the thermal infrared, this error can reach 10°C at 3.74 μm, but is negligible in bands 4 and 5 around 11 μm.

The infrared radiation emitted by the surface is partially absorbed in the atmosphere, mainly by water vapor. This absorption lowers the brightness temperatures measured by the satellite. The spectral bands of the AVHRR correspond to "windows" at which the radiation is least absorbed. In tropical regions, where the moisture content of the atmosphere reaches 60 kg/m^2, the errors due to absorption are still about 10°C in band 5, 7°C in band 4 and 3°C in band 3. Surface temperatures are then estimated using empirical multispectral corrections (McClain *et al.*, 1985). Since moisture content in dry subtropical regions such as Southern California is typically ~10 kg/m^2, corresponding to a brightness temperature error less than 1°C for band 4, this band was chosen and the water vapor correction was neglected in this preliminary study.

3. Comparison with air temperatures

Seven images correspond to an intensive experiment during which hourly data from 44 meteorological stations and 4-hourly data from 11 sounding stations were recorded (Project BASIN, August 8 to 10, 1984; Wakimoto and Wurtele, 1984). Surface temperature co-located with the stations were extracted from the images. Cloudy pixels were rejected using the radiance difference between 3.7 μm and 10.8 μm for night images, and the near-infrared reflectance for daytime images. Stations at an altitude higher than 400 m such as Mt. Wilson were also rejected to avoid the problem of relating pixel-average temperatures with point data taken in rough terrain.

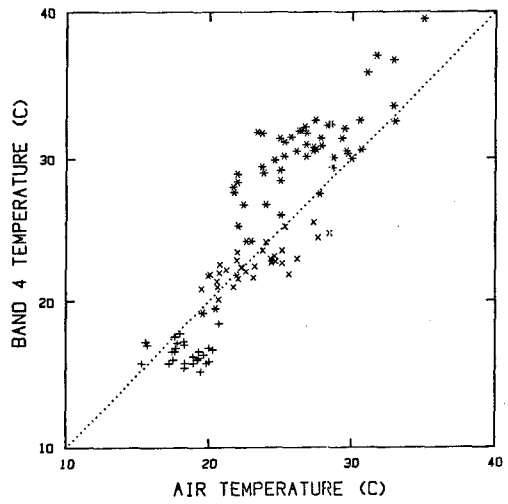

Fig. 3. Scatter plot of satellite temperature versus air temperature for NOAA-6 at 08:15 and 19:00 (+) and NOAA-7 at 04:00 (×) and 16:00 (*).

Table 1. Mean and standard deviation σ of the difference between satellite and air temperatures at different times of the day.

time	symbol	mean	σ	# points	# images
04:30	+	0.0°C	1.6°C	29	3
07:00,19:00	×	1.1°C	1.5°C	34	2
15:30	*	5.4°C	2.3°C	54	2

Fig. 3 is a scatter plot of satellite temperature versus surface air temperature for all the satellite images; the corresponding statistics are shown in Table 1. At night, the satellite temperatures are in good agreement with air temperatures; the standard deviation of the difference is 1.6°C (to provide a reference, comparisons between corrected satellite temperatures and ocean surface temperatures have a typical scatter of ~0.6°C; Bernstein, 1982). In the afternoon, satellite temperatures are about 5.4°C warmer than the air. The standard deviation is 2.3°C.

The standard deviations are remarkably small given the fundamental difference between pixel-averaged surface temperatures and point measurements of air temperature. The diurnal cycle of the mean difference is in qualitative agreement with simple planetary boundary layer models, which predict the largest difference in the early afternoon when the incoming solar radiation is most intense. The larger standard deviation at 15:30 reflects more turbulent conditions in the afternoon, as evidenced by peak-to-peak fluctuations of 1.5°C over less than 10 minutes observed at a meteorological station in downtown L.A.

4. Cloud statistics

During the day, cloudy pixels were flagged when band 2 exceeded a threshold based on the histograms of cloud-free images. At night, cloudy pixels were flagged when the difference between band 3 and band 4 exceeded a threshold based on the histograms of cloud-free images (the emissivity of clouds is 0.70 at 3.7 μm versus 0.99 at 11 μm). Examples of histograms of cloud-free and cloud-covered images are shown in Fig. 4. The brightness temperatures in band 4 was used to differentiate between low (stratus) clouds and high (convective) clouds. Maps of cloud probability were then constructed for each set of images at the average times of satellite passage shown in Fig. 1.

At ~03:40 average local time (Fig. 5), stratus clouds cover the ocean and the coast in 80% of the images and in 40% to 60% penetrate over the low-altitude Los Angeles basin to the edge of the San Gabriel mountains and to San Bernardino valley. These low clouds do not occur over the mountains and in the Mojave desert. Similar patterns are seen at ~07:40 (not shown), when stratus clouds cover the ocean and the coast in 30 to 40% of the images and in 10 to 20% extend over the basin. At ~15:10 (Fig. 6), low clouds have dissipated and high clouds are found in 15% to 20% of the images over the mountains and the desert, but in less than 3% over the basin. At ~18:50 (not shown), low clouds have formed again over the ocean in 10 to 25% of the images and in 5 to 15% extend over the basin.

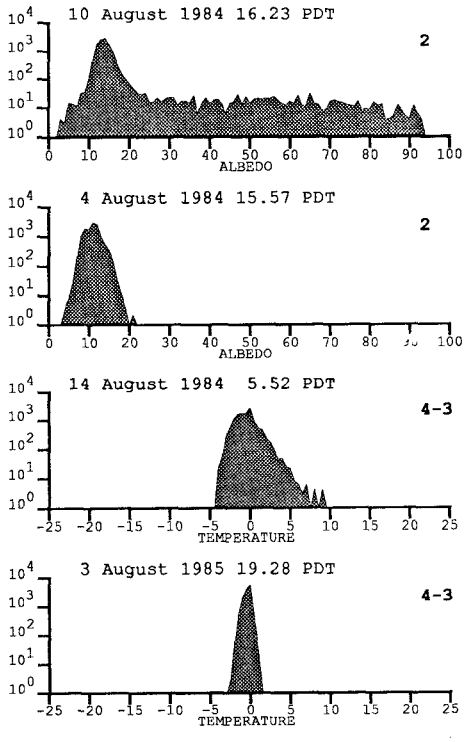

Fig. 4. Histograms used for cloud classification. (a) albedo of a partially cloudy daytime image, (b) albedo of a cloudless daytime image, (c) band 4 - band 3 of a partially cloudy night image, (d) band 4 - band 3 of a cloudless night image.

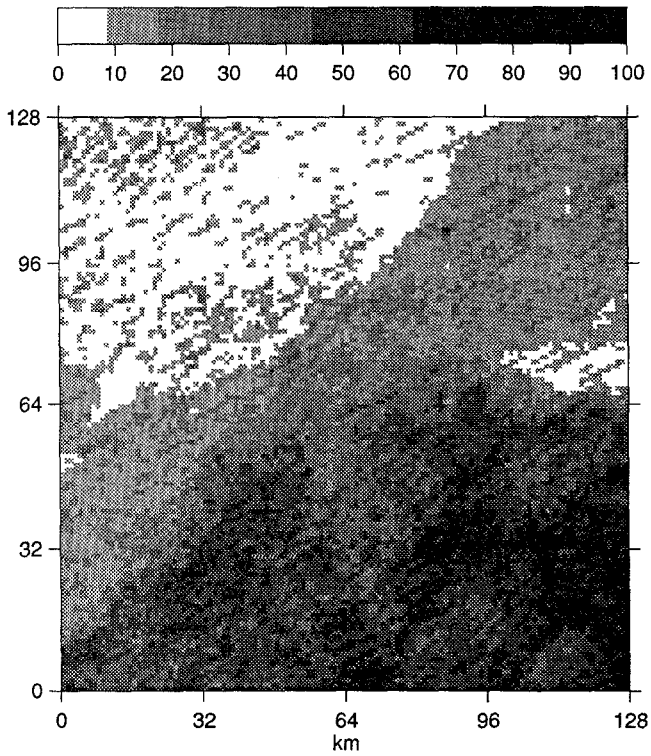

Fig. 5. Probability of cloud occurrence at ~03:40 local time.

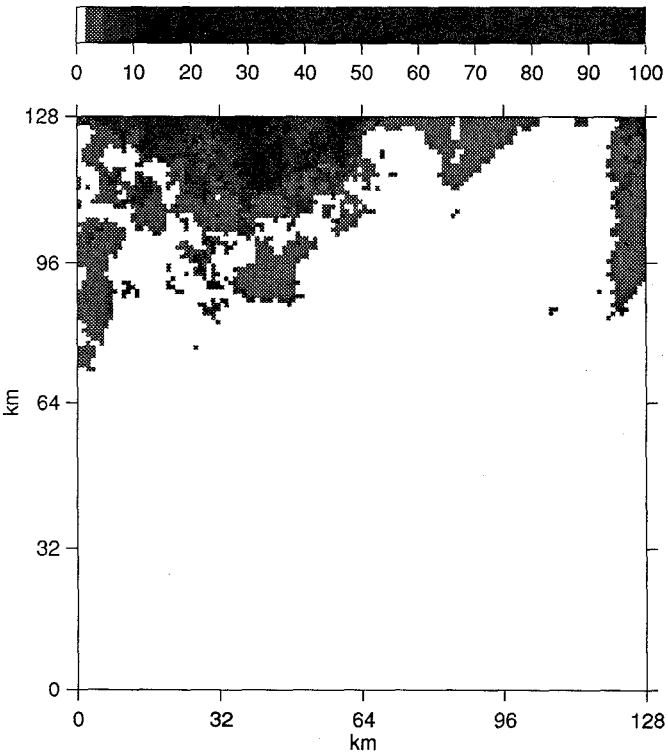

Fig. 6. Probability of high cloud (T < 0°C) occurrence at ~14:40 local time.

These cloud patterns corresponds to the mesoscale climate of the region. A deck of marine stratus form over the ocean when warm moist marine air masses are advected over cold coastal water, and fills the entire low-altitude basin. The maximum elevation reached by the stratus deck in the 03:40 and 07:40 images is about 600 m, consistent with the reported 300 to 600-m thickness of the marine layer (Elford, 1970).

5. Temperature statistics

Maps of average surface temperature were constructed for each set of images at the different times of satellite passage (Fig. 1). Because the rate of change of surface temperature is large in the afternoon, separate averages were computed for 1984 (~15:10 local time) and 1985 (~13:55), but the two years were combined for 03:40, 07:40 and 18:50. Pixels flagged as cloud in the previous section were omitted from the average, and average pixels with a cloud probability larger than 75% were discarted (they appear as a white mask over the ocean in Fig. 8).

At 15:10 (Fig. 7), the ~1800-m high San Gabriel mountains are 12°C colder than the low-altitude basin. Valleys are seen as warmer features crossing the mountain range (e.g. near [64,96] km). Coastal relief such as the Santa Monica and Santa Ana mountains are also colder than the basin. Surface temperatures exceeds 33°C in San Fernando valley, San Bernardino valley and the Mojave desert.

The San Andreas fault can be seen as a cold anomaly crossing the desert near [0,96] km. Other cold spots in the desert correspond to irrigated fields, which were identified in a multispectral Landsat image. Higher temperatures are found downtown L.A. near [45,45] km, and in the industrial area of Long Beach near [64,32] km.

At ~03:40 (Fig. 8), the south flanks of the Santa Ana and San Gabriel mountains are in general ~3°C *warmer* than San Fernando and San Bernardino valleys (e.g. near [50,75] km, or [120,70] km), despite their higher altitude. The causes of this effect are not understood. Warmer temperatures are also found in downtown L.A. and around Long Beach, presumably reflecting nocturnal heat islands, the contour of which closely follows contours of building density obtained from a Landsat image. The San Andreas fault appears as a warm anomaly. Small details such Interstate 10 running parallel to the San Gabriel mountains (from [69,78] km to [105,114] km) are distinctly warmer than the background.

To further illustrate these temperature variations, a profile of average temperatures from LAX Airport to the Mojave desert through downtown L.A. is shown in Fig. 9. The correlation with topography is clear. Heat islands in downtown L.A. (at 20 km from the coast) and South Pasadena (at 40 km) are noticeable. The transition from ocean to land is spread over ~2 km, as should be expected given the ~2-km rms geolocation error.

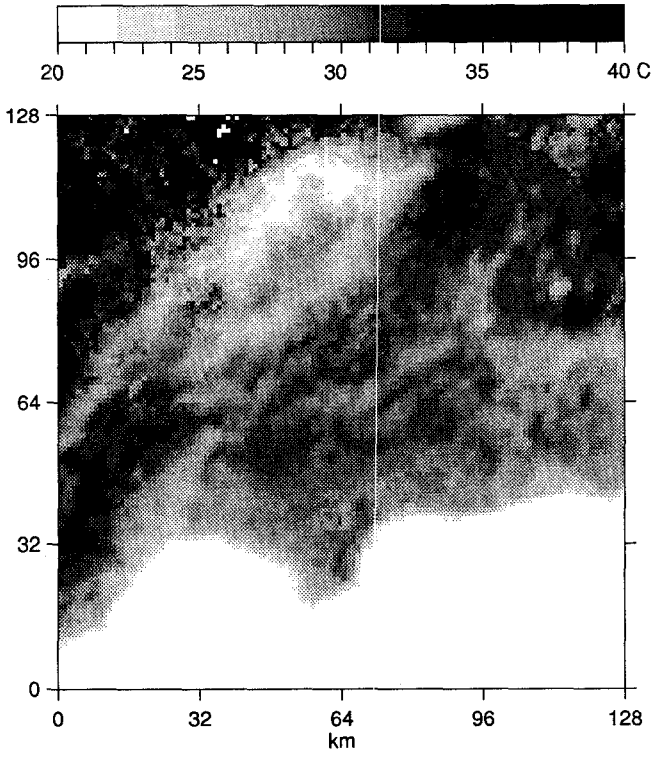

Fig. 7. Average temperature of cloudless pixels from 18 images measured around 15:10 in August 1984.

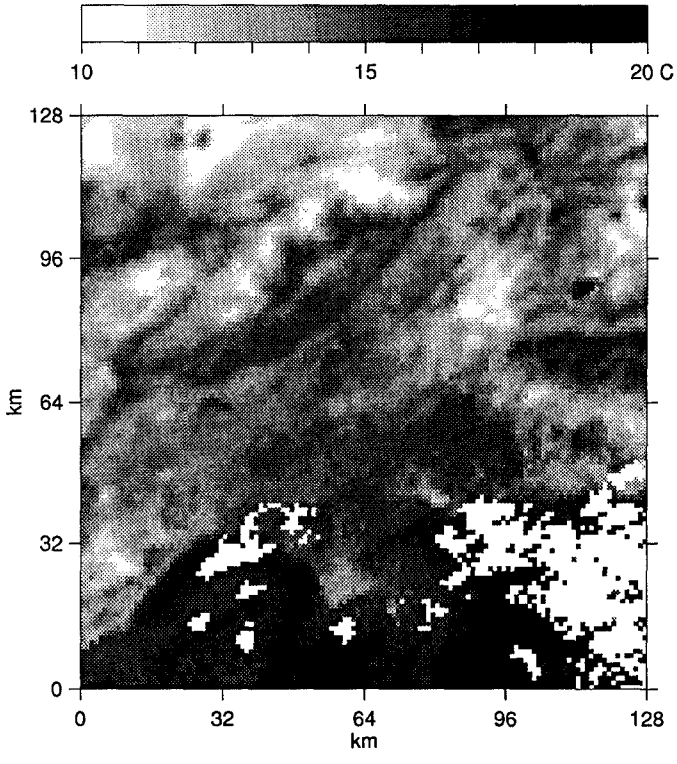

Fig. 8. Average temperature of cloudless pixels from 11 images measured around 03:40 in August 1984 and 1985.

The difference between the 15:10 and 03:40 average temperature maps is shown in Fig. 10. The amplitude is less than 5°C over the ocean and Perris lake, ~10°C over the mountains, ~15°C over the basin, and reaches 25° in the west of San Fernando Valley, the east of San Bernardino valley, and in the Mojave desert.

6. Conclusion

We have demonstrated that statistics of series of accurately co-registered satellite infrared images yield a wealth of informations on micro-climatic processes at a scale of a few kilometers. Although for this preliminary study we chose a very simplified treatment of atmospheric absorption, surface emissivity and cloud detection, the qualitative aspects of the temperature and cloudiness maps, such as amplitude of the diurnal cycle, positions of urban heat islands and distribution of cloud types should not be affected.

Future work will improve the treatment along the following lines:

(i) the error due to the absorption of infrared radiation by water vapor in the atmosphere will be computed directly from radio-sonde data using an atmospheric transmittance model such as LOWTRAN (Kneizys *et al.*, 1980); this will provide an estimate of the emissivity difference between bands 4 and 5;

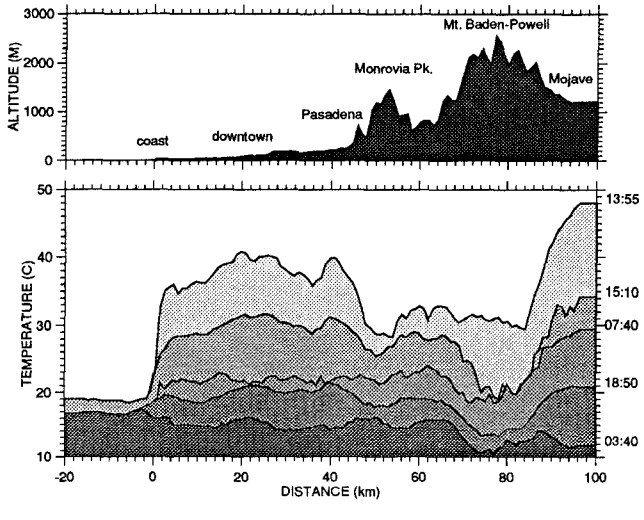

Fig. 9. Bottom: average profiles of surface temperature across the Los Angeles basin from 33°45N 118°41W to 34°27N 117°36W, at ~03:40 (11 images), ~07:40 (21), ~13:55 (15), ~15:10 (18) and ~18:50 (19). Top: corresponding digital topography. Salient geographic features are indicated.

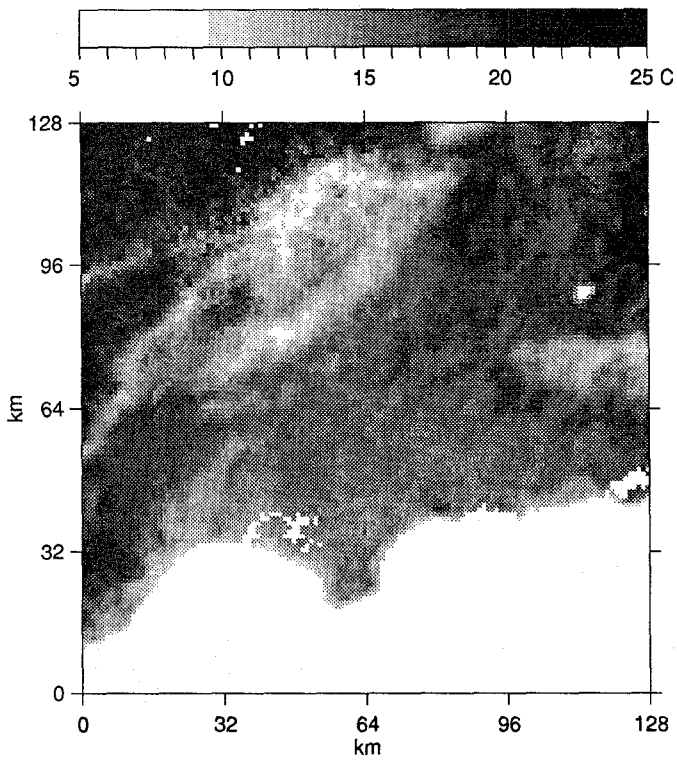

Fig. 10. Difference between the average temperatures shown in Fig. 7 and 8.

(ii) the cloud-detection algorithm will be improved by comparing the albedo of each pixel with the average clear albedo, allowing a better differentiation between white sands and thin stratus or sub-pixel cumulus clouds, which may be missed by the threshold technique used here;

(iii) the observed difference between air and surface temperature will be compared with the predictions of a planetary boundary layer model forced by the meteorological data available from project BASIN.

Microclimatic statistics such as those presented here have direct applications to urban planning and building design. First, a better understanding of urban heat island effects may help control them when planning new neighborhoods, by selecting the albedo of roofs, the clustering of buildings and the distribution of green areas. Second, these statistics provide high resolution climatic data needed when designing energy-efficient constructions.

References

Bernstein, R.L., "Sea surface temperature estimation using the NOAA-6 satellite AVHRR," *J. Geoph. Res.*, vol. 87, pp. 9455-65 (1982).

Buettner, K.J.K. and C.D. Kern, "The determination of infrared emissivities of terrestrial surfaces," *J. Geoph. Res.*, vol. 70, pp. 1329-37 (1965).

Dousset, B., "Some applications of satellite thermal infrared images to urban climatology," in *Proc. 10th Congress of the International Council for Building Research*, pp. 3150-3159, National Bureau of Standards, Gaithersburg (1986).

Elford, C.R., "Climates Of The States: California," *Climatography of the United States*, vol. 60-4, pp. 86-94 (1959).

Kneizys, F.X., E.P. Shettle, W.O. Gallery, J.H. Chetwynd, L.W. Abreu, J.E. Selby, R.W. Fenn, and R.A. McClatchey, "Atmospheric transmittance radiance: computer code Lowtran-5," TR-80-0067, p. 233, Air Force Geophysics Laboratory, Cambridge, 1980.

McClain, E.P., W.G. Pichel, and C.C. Walton, "Comparative performance of AVHRR-based MCSST," *J. Geoph. Res.*, vol. 90, pp. 11587-601 (1985).

Wakimoto, R.M. and M.G. Wurtele, "Project BASIN," *Bull. Am. Met. Soc.*, vol. 65, pp. 1210-11 (1984).

Acknowledgements. The authors thanks B. Givoni, M. Wurtele, and P. Flament for helpful discussions during the course of this research. R. Bernstein supplied some of the images. D. Kelley provided an outstanding plotting package. This work was funded by the California Space Institute through grant CS-78-86. Additional support was provided by the International Federation of University Women in Geneva and by a B.A. Berkus Systems Building and Housing Research fellowship.